Article

Cl-Doped ZnO Nanoparticles with Enhanced Photocatalytic Activity via Selective Surface Lixiviation: Implications for Acetaminophen Degradation

Gustavo M. Fortes, Andre Luiz da Silva,* Bruno Ramos, Jefferson Bettini, Fabio Coral Fonseca, Renato V. Gonçalves, Orlando Rodrigues Junior, and Douglas Gouvea

Read Online

ACCESS | Metrics & More | Article Recommendations | SI Supporting Information

ABSTRACT: Selective surface lixiviation is commonly employed to quantify dopants segregated on the surface of nano oxides. In this study, we utilize this method as a strategy to enhance the photocatalytic activity of Cl-doped ZnO. Diffuse reflectance spectroscopy revealed that the dopant was not dissolved in a solid solution, and surface defects were confirmed through color measurements using the CIE Lab* system and electron paramagnetic resonance (EPR). X-ray photoelectron spectroscopy (XPS) and diffuse reflectance infrared Fourier-transform spectroscopy (DRIFTS) confirmed the presence of $ZnCl_2$ on the surface of doped ZnO samples. STEM EDS elemental mapping revealed an ∼6 nm-thick Cl-enriched surface layer at the edge of the ZnO nanoparticle. The selective lixiviation method effectively removed the Cl dopant from the surface of ZnO nanoparticles, as demonstrated by FTIR-DRIFT, while preserving the additive in the grain boundaries (GBs). This process mitigated chloride poisoning during photocatalysis by removing soluble Cl and enhancing electrical conductivity through GB segregation. These synergistic effects contributed to the improved photodegradation of the model contaminant acetaminophen, positioning lixiviated Cl-doped ZnO nanoparticles as highly effective for the target application of acetaminophen degradation.

KEYWORDS: selective surface lixiviation, ZnO, interface segregation, electrical properties, photocatalytic activity, grain boundaries
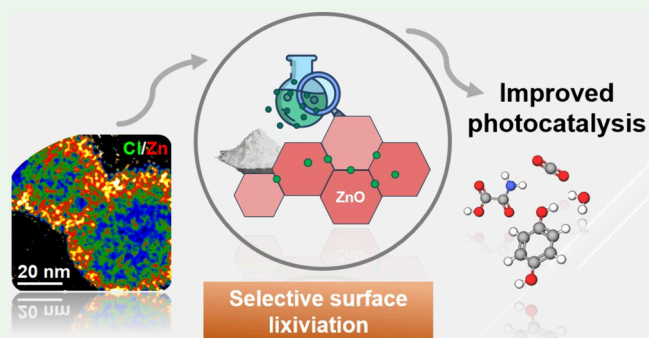
1. INTRODUCTION

In recent years, there has been a surge in the development of metal oxide-based semiconductor materials for photocatalysis, from the ubiquitous TiO_2 to more exotic inner transition metal oxides, such as ThO_2.[1] The key driving force behind this exploration of the periodic table is the search for materials with superior electronic transfer capacity and band energy positions compatible with the target catalytic reactions. The most common approach to preparing new photocatalysts is the incorporation of a foreign species (a dopant) into a well-known photocatalyst, such as TiO_2,[2] ZnO,[3] or WO_3.[4] A key limitation of most studies in the field is the lack of comprehension of where the dopant is located within the material domain. This information is not only important to explain the mechanism behind eventual activity enhancements but also essential to draw roadmaps for future improvements. Within this context, the selective lixiviation method is a procedure that has been recently proposed and used to quantify dopants segregated on the surface of nano oxides.[5−14] The method relies on the solubility difference between the matrix (the host oxide) and the solute (the dopant itself). It was initially developed as a technique to quantify surface

excess, that is, surface segregation; however, in this article, we explore its use as a tool to enhance the catalytic properties of photocatalytic nano oxides.

The surface segregation of dopants is intrinsically connected to the thermodynamic stability of the nanoparticles, which is governed by the surface energy term, and has been used as an efficient tool to enhance nanoparticle stability.[15] Its occurrence is directly related to the segregation enthalpy, which can be attributed to four driving terms in polycrystalline materials: (i) the difference between the surface energies of the solute and the solvent; (ii) an elastic solute strain energy directly influenced by the difference in the ionic radius between the host and dopant ions; (iii) the solute−solvent interaction; and (iv) charge compensation and electrostatic potential.[5,6] The energy of the system is minimized by the segregation of dopant
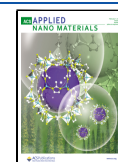
ions to more energetic interfaces, which can be surfaces (e.g., solid−gas or solid−liquid interface) or grain boundaries (a solid−solid interface, GBs), both impacting the overall charge conductivity of the system.

Nanostructured zinc oxide (ZnO) was the chosen material for the present study. It is among the most well-known polycrystalline semiconductors for technological applications. As an intrinsic n-type semiconductor, electrons are the main charge carriers due to the formation of oxygen vacancies ($V_O^{\cdot}$) ($O_O^{\times} = 1/2\ O_2(g) + V_O^{\cdot\cdot} + 2e'$) and interstitial zinc ($Zn_i^{\cdot\cdot}$) sites ($Zn_{Zn}^{\times} + O_O^{\times} = Zn_i^{\cdot\cdot} + 2e' + 1/2\ O_2(g)$).[16−18] Wurtzite, the most common phase of ZnO, has an electronic configuration that results in a direct band gap. ZnO is used as a base material to prepare catalysts for different chemical processes, for example, $Cu/ZnO/Al_2O_3$ composites have been widely used for more than 50 years in the industrial production of methanol, and pure ZnO has been investigated to develop a greener synthetic route using CO_2 and H_2O as precursors.[19]

One of the promising strategies to enhance the photoactivity of nanoparticles, such as ZnO, is to improve their electrical properties. Approaches to tailor this property include modifications by doping, including transition metals such as Mo,[20] and anions such as Cl.[21−25] Anionic doping presents key advantages for photoelectric enhancements:[26−29] it is considered a better route to improve charge mobility while concurrently avoiding photonic losses. This occurs because the conduction band (CB) of semiconductors is composed of the d-orbitals of the metal species, and the incorporation of other cations can cause a disturbance in the CB, leading to an increase in scattering events, and hence a decrease in mobility and conductivity. Conversely, since the valence electrons in anions are localized in p-orbitals, the perturbation is restricted to the valence band of the semiconductor, and the scattering of conduction electrons is minimized.[30]

One drawback of using Cl ions in the photocatalytic process is catalyst deactivation due to the formation of zinc chloride ($ZnCl_2$) on the surface of the nanoparticles, a phenomenon known as chloride poisoning.[31] The surface-segregated Cl sterically blocks the adsorption of organic molecules, inhibiting the photoactivity while consuming the photogenerated holes, hindering the formation of highly reactive oxygen species that are responsible for the oxidation of organic pollutants.[32] Thus, this work aims to use the selective lixiviation method as a tool to remove most of the Cl from the surface, reducing the chloride poisoning effect while preserving the Cl in the GB to enhance electronic conductivity, hindering e^-/h^+ recombination, and improving the photoactivity. While the method has broader potential for various photocatalytic applications, this work specifically focuses on the photodegradation of acetaminophen as the target application.

2. EXPERIMENTAL PROCEDURE

2.1. Synthesis of Cl-Doped ZnO Nanopowders. The polymeric precursor method, known as Pechini, was used to synthesize ZnO nanopowders.[33] 45.8 wt % anhydrous citric acid (Synth, $C_6H_8O_7$, ≥99.00 wt % purity), 30.5 wt % ethylene glycol (Synth, $C_2H_6O_2$, ≥99.00 wt % purity), and 23.6 wt % hydrated zinc nitrate (Synth, $Zn(NO_3)_2 \cdot 6H_2O$, ≥99.98 wt % purity) were used to prepare the precursor resin, the latter being the zinc source. The dissolution of the anhydrous citric acid and zinc nitrate into ethylene glycol was carried out at 70 °C until a completely homogeneous and transparent solution was obtained. Next, the temperature was raised to 120 °C to promote polymerization and eliminate volatiles from the nitrates. The introduction of chloride (Cl) doping was made by

adding determined amounts of aqueous solutions of NH_4Cl (Synth, 99.50 wt % purity) to the resin. The molar concentrations of Cl in the doped materials were targeted as x = 1.0, 3.0, and 6.0%. An undoped sample was also synthesized. The corresponding samples used in this study were labeled ZnO (undoped) and ZnO-xCl. The prepared precursors were then calcined in two steps. The first aimed to decompose organic traces, the samples were treated at 360 °C for 5 h. Subsequently, a mortar and pestle was used to manually grind the powders, and the second calcination was carried out at 360 °C for 15 h. Both steps were performed under constant airflow.

2.2. Powder Characterization. Powder X-ray diffraction (XRD) patterns were collected using an X'Pert-MPD (Philips) diffractometer with Cu Kα radiation (λ = 1.5406 Å), operated at 45 kV and 40 mA. Data were collected in the range of 5−70°, with a step size of 0.02° 2θ per second. Rietveld analysis was used to estimate the crystallite sizes and lattice parameters using X'Pert Highscore software, with $MgAl_2O_4$ as the standard. In the refinement, the average crystallite size was utilized, as the goal was to evaluate the overall effect of the additive on the nanostructure. ZnO exhibits anisotropy due to its lack of local symmetry; however, this does not significantly impact the average crystallite size, which was also measured by transmission electron microscopy.

Specific chloride ion-selective electrodes (ISE) from Hanna Instruments were used to measure the Cl content of the samples. The samples were dissolved in a 1 N sulfuric acid solution, followed by neutralization using a suitable amount of a 2 M KOH solution to regulate the pH of the sample according to the operational range of the electrode.

The density of the powders was measured with a Micromeritics AccuPyc II 1340 He gas pycnometer. For proper degassing, the experiment was carried out after 200 purges. Surface area measurements were carried out using the Brunauer−Emmett−Teller (BET) method with nitrogen gas (N_2) adsorption at 77 K (Micromeritics Gemini III 2375). Before the experiment, the powders were degassed at 300 °C for ~12 h in a VacPrep 061 (Micromeritics). Lixiviated samples were also pretreated for 12 h under vacuum but at 150 °C to avoid redistribution of dopants through interfaces.

A Shimadzu UV-2600 spectrometer, fitted with an integrating sphere, was used to record the diffuse reflectance spectra (DRS) of the samples. Color measurements were performed by a MiniScan XE Plus equipment using the CIE $L*a*b*$ system and the standard illuminant D65. For this experiment, the ZnO nanopowders were pressed into cylindrical pellets, 35 mm in diameter and 11 mm in thickness, using a Carver hydraulic press at 125 MPa.

The surface electronic characteristics of the samples were examined by X-ray photoelectron spectroscopy (XPS). The analysis was performed by employing a Scienta Omicron ESCA+ apparatus with an Al Kα source, while charge compensation was achieved using a low-energy electron flood gun. High-resolution spectra were acquired with a pass energy of 30 and 0.05 eV energy increments. The reference point for XPS spectra calibration was established based on the binding energy of adventitious carbon (C−C/C-H bonds at 284.8 eV). Data analysis was carried out by utilizing CasaXPS software.

EDS measurements were conducted in a Titan Themis Cubed (Themo Fischer) equipped with four energy-dispersive spectroscopy (EDS) detectors. The measurement was carried out in the STEM mode. The probe size used was 0.15 nm; the pixel size for the EDS image spectrum was 0.2 nm; and the total pixel time acquisition was 0.32 s.

2.3. Selective Surface Lixiviation, DRIFTS, and EPRs. Chloride segregation on the surface of ZnO was verified using the selective lixiviation method.[5,6,8−10,34] In brief, this method consists of ultrasonicating ~200 mg of nanoparticles dispersed in ~1.8 g of distilled water for 1 h. The suspension is centrifuged twice at 13,000 rpm (10,390 G) for 15 min to separate the powder from the solution, allowing quantification of the ions dissolved in the solvent. The supernatant is collected (~1.4 g), and the dopant content is measured with a Cl-specific ISE. The schematics of this method are shown in Figure 1. The hexagons in the left-hand corner represent the ZnO nanoparticles before lixiviation. The dark green dots represent Cl ions
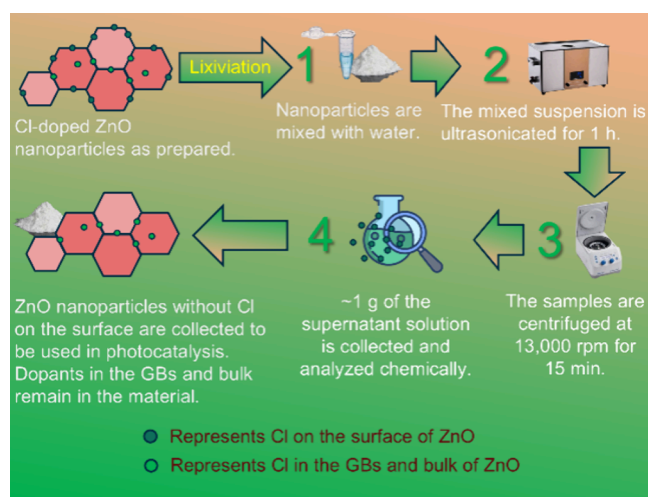
Figure 1. Schematic of the selective surface lixiviation method.

segregated on their surface, while the light green dots represent Cl ions segregated in the GBs or dissolved in the oxide matrix. The procedure is divided into four steps: (i) the nanoparticles are mixed with water, used as the solvent since it can solubilize Cl but not Zn; (ii) the mixed suspension is ultrasonicated for 1 h to facilitate the transport of Cl from the ZnO surface to the solution; (iii) the samples are centrifuged at 13,000 rpm for 15 min to promote the separation of the powder; and finally, (iv) in the last step, ~ 1 g of the supernatant solution is collected and analyzed.

The diffuse reflectance infrared Fourier-transform (DRIFT) spectroscopy analyzed the functional groups adsorbed on the surface of the nanopowders by using a Shimadzu IRTracer-100 spectrometer. DRIFT spectra were recorded from 400 to 4000 cm^{-1} with 4 cm^{-1} resolution.

The paramagnetic response of ZnO nanopowders was assessed by using electron spin resonance (EPR) spectroscopy. The measurements were conducted at room temperature and 100 K using an X-band EPR spectrometer (Bruker EMX PLUS). The parameters used were as follows: 100 kHz field modulation frequency, 2.0 mW microwave power, 3370 G center field, 400 G sweep width, 4.0 G modulation amplitude, 81.9 ms time constant, and 10 scans. Room temperature measurements were performed at 20 °C in a controlled humidity environment.

2.4. Electrical Measurements and Photocatalytic Reactions. The electrical transport properties of the samples studied were analyzed by electrochemical impedance spectroscopy (EIS) measurements. The samples were compressed into cylindrical pellets, 35 mm in diameter and 11 mm in thickness, by uniaxial pressing (125 MPa). Then, the pellets were heated to 370 °C for 1 h to improve the contact among the grains. A high-purity silver paste (EMS Silver Conductive Coating, EMS #12684-15) was carefully deposited, precisely covering the surface of the cylindrical pellets and preparing the contact pads in the Ag/Cl−ZnO/Ag symmetric cell configuration. The silver paste applied was then cured at room temperature for more than 24 h, following the manufacturer's recommendation. EIS data were collected with an impedance meter and gain-phase analyzer (Novocontrol Alpha-A analyzer) in a frequency range from 10^7 to 1 Hz with an amplitude of 500 mV AC voltage. Electrical contact in the EIS sample holder was made by platinum leads, and temperature was measured using a type K thermocouple located next to the three samples. The sample holder was placed into a gastight alumina tube inside a tube furnace. To ensure that the samples were free of H_2O and CO_2 on the surface, the pellets were treated at 200 °C under synthetic air flux (~10 mL min^{-1}). EIS data were measured under (dry) synthetic air flow on cooling at 200, 175, 150, 125, and 100 °C. Before EIS measurements, the samples were kept for ~30 min at each programmed temperature for thermal stability. The total electrical conductivity was calculated by fitting the EIS diagrams, normalized to the geometric factors of the specimens.
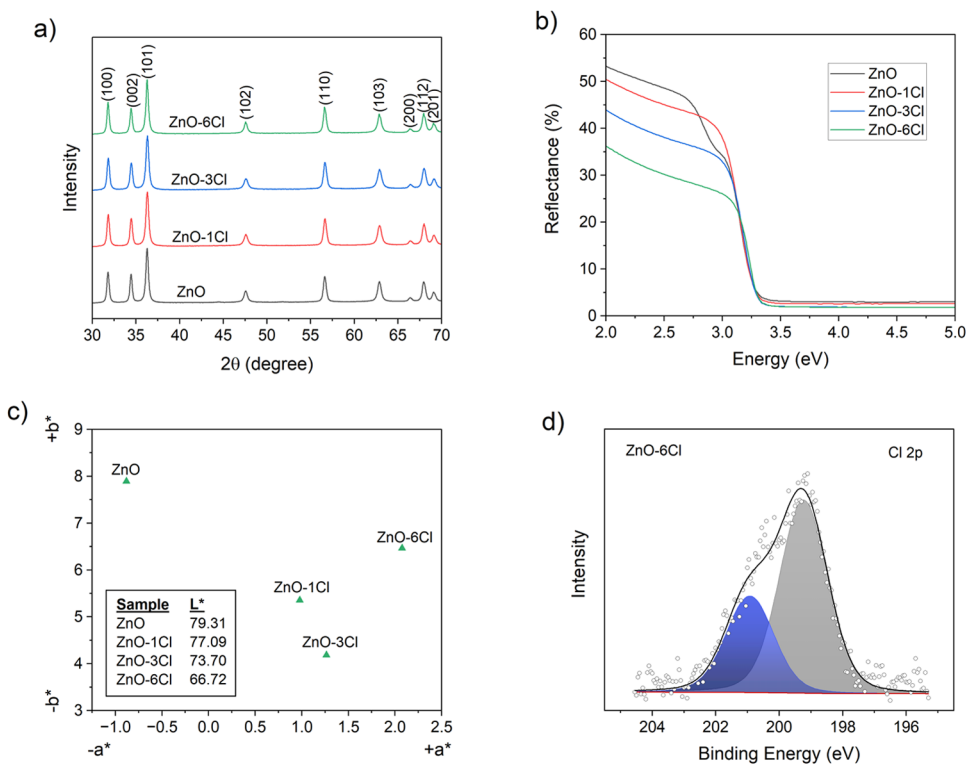

Figure 2. Characterization of ZnO and Cl-doped ZnO samples. (a) X-ray diffraction patterns of ZnO, ZnO-1Cl, ZnO-3Cl, and ZnO-6Cl samples. (b) Diffuse reflectance spectroscopy (DRS) analysis showing the reflectance as a function of energy for all samples. (c) CIE Lab* color system illustrating the color variations induced by Cl doping. (d) Cl 2p XPS spectrum for the ZnO-6Cl sample, confirming the presence of chlorine.

Table 1. Total Cl Content, Crystallite Size, Density, SSA, TSA, SGB, and SGB/SSA Ratio of ZnO and Cl-Doped ZnO Samples

sample	total Cl content (mol %)	crystallite size (nm)	density (g/cm³)	SSA[a] (m²/g)	TSA[b] (m²/g)	SGB[c] (m²/g)	SGB/SSA
ZnO	0.07 ± 0.01	29.7 ± 0.6	5.45 ± 0.01	13.6 ± 0.1	43.9 ± 0.9	15.1 ± 1.0	1.11 ± 0.08
ZnO-1Cl	0.43 ± 0.04	27.2 ± 0.5	5.47 ± 0.01	14.4 ± 0.1	47.8 ± 0.8	16.7 ± 0.9	1.15 ± 0.07
ZnO-3Cl	1.03 ± 0.09	25.8 ± 0.4	5.44 ± 0.01	16.9 ± 0.1	50.6 ± 0.9	16.8 ± 1.0	0.99 ± 0.06
ZnO-6Cl	1.25 ± 0.11	29.8 ± 0.6	5.41 ± 0.01	16.7 ± 0.1	44.2 ± 0.9	13.7 ± 1.0	0.82 ± 0.06

[a]Specific surface area, as measured by N_2 adsorption using the BET theory. [b]Total surface area, as calculated using eq 1. [c]Specific grain boundary area, as calculated using eq 2.

The photocatalytic performance of the undoped ZnO and the nonlixiviated and lixiviated Cl-doped ZnO samples was performed as follows. In a borosilicate glass test tube, 5 mg of the powder samples was suspended in 4 mL of a 5 ppm acetaminophen (ACT) solution prepared in deionized water. The tube was irradiated by a UV-A LED chip (peak emission at 370 nm), which provided an irradiance of 4.2 mW cm^{-2} on the outer walls of the test tube, positioned 10 cm from the light source. 100 μL aliquots were collected periodically, diluted, filtered, and stored under refrigerated conditions before analysis. ACT was quantified by UPLC (20-AF, Shimadzu Co.), as described elsewhere.[7,35]

3. RESULTS AND DISCUSSION

3.1. Characterization of the Nanopowders. The X-ray diffraction (XRD) patterns for undoped and Cl-doped ZnO samples are listed in Figure 2a. The presence of broad peaks in all samples indicates the nanosized nature of the crystallites. The only phase observed is wurtzite (JCPDS card no. 36-1451), which confirms the purity of the samples. The ratio of the peaks for the (002) and (100) planes changed slightly for the Cl-doped samples compared to the undoped ZnO. This change suggests enhanced stability of the facet oriented along the (100) plane relative to the (002) plane, likely resulting from the preferential surface segregation of Cl ions.

To provide a precise interpretation of the results presented in this study, the total Cl contents left in the ZnO samples after calcination were measured by ISE. The results are shown in Table 1. The higher the Cl added, the greater the amount retained in the samples. However, higher Cl dosages retained proportionally less, demonstrating a saturation of around 1.0 mol % of Cl, which is consistent with previous studies.[34] Cl losses are usually caused by evaporation during the calcination stages. Undoped ZnO also showed traces of Cl, which likely arise from impurities present in the precursors used in the synthesis.

The average crystallite sizes of the undoped and Cl-doped ZnO nanopowders, calculated by Rietveld refinement of the XRD data, are presented in Table 1. All synthesized nanopowders showed crystallite sizes smaller than 30 nm. Unlike usually seen for cation dopants,[6,8,36−40] the crystallite sizes did not increase proportionally to the amount of added Cl. Although the crystallite sizes did not show a clear trend, the size variation observed for ZnO-1Cl and ZnO-3Cl samples may be related to the synthesis processing steps, where the evaporative loss of Cl ions, its bulk solubilization, and segregation affect the interfacial energy of the samples,[41] causing variations in the crystallite sizes.

The density, specific surface area (SSA), total specific area (TSA), specific grain boundary (SGB) area, and SGB/SSA ratio are also presented in Table 1. Cl doping caused a general reduction in the pycnometric density, which may be related to the formation of point defects, such as zinc vacancies (V_{Zn}'').[42] However, as observed for the crystallite sizes, there is no clear dependence on the amount of dopant.

The SSAs, obtained by N_2 adsorption, correspond to the solid−gas interface. The values increased with increasing amounts of Cl, which might be an indication of surface segregation. For a better interpretation of the dopant distribution, the TSA, SGB, and SGB/SSA ratios must be analyzed together. The TSA is calculated using eq 1, which assumes a truncated octahedron shape, where d is the average crystallite size, and ρ is the measured density. The SGB area is calculated according to eq 2.[43]

$$TSA = \frac{7.11}{d \cdot \rho} \tag{1}$$

$$SGB = \frac{(TSA - SSA)}{2} \tag{2}$$

The TSA and SGB areas do not follow the progressive amount of Cl measured. This behavior indicates variations in the distribution of the dopant during the crystallization process, and consequently, variations in the energy balance of the interfaces. Conversely, the SGB/SSA ratio presented a direct correlation with the amount of dopant. The SGB/SSA ratio decreased as the amount of Cl increased, suggesting an improved stabilization of the surface (solid−gas interface) with respect to the GB (solid−solid interface). It seems that Cl segregates preferably on the surface of the nanoparticles.

Sample ZnO-6Cl does not strictly follow the trend observed for samples ZnO-1Cl and ZnO-3Cl in Table 1 (crystallite size, TSA, and SGB). This difference arises from high saturation and a strong excess of the additive at the interfaces. When a small amount of the cation dopant is added to a nano-oxide matrix, it generally segregates preferentially at the grain boundaries.[5,44] However, with larger amounts of the additive, while segregation at the grain boundaries continues, there is a proportionally greater segregation on the surfaces. Once the interfaces reach saturation, the additive exudes to form a second phase,[8] which, in the case of chlorides, results in the formation of volatile species.[34]

The pieces of evidence seen so far indicate that the incorporated Cl is mainly segregated on the surface of the ZnO nanoparticles, which should not affect the band gap energy. To verify this information, the band gap energies of the samples (Figure S1) were calculated from UV−visible diffuse reflectance data using the Tauc model (Figure 2b).[45] Details about the methodology and calculations can be found in the Supporting Information. The band gap energies did not change with the addition of Cl ions, and the values were all ∼3.16 ± 0.1 eV, which indicates that Cl doping did not significantly change the bulk lattice.

Although the band gap energies did not change, a decrease in reflectance was observed for energies below ∼3.0 eV. This decrease is normally associated with surface defects, which cause color changes. Following this information, color measurements using the CIE L*a*b* system were performed.

The results are shown in Figure 2c and indicate a gradual shift to purple, that is, positive $a*$ and negative $b*$, while $L*$ decreases, suggesting that the powders are becoming darker. Three mechanisms are usually responsible for color changes in oxide materials: (i) charge transfer between ions and defects, (ii) introduction of a donor or acceptor level in the band gap by defects, and (iii) the presence of color centers generated by electron transfer from the semiconductor lattice to defects on the surface.[46] Considering that the band gap energies did not change among the samples, it is likely that this change was caused by defects on the surface of the nanoparticles. To better visualize the color differences between undoped and doped samples, the perceptual distances, ΔE, were calculated using ZnO as the standard. The perceptual distance provides a measure of how far apart, or rather, how much contrast exists between two colors. ΔE was calculated according to eq 3, and the results are presented in Figure S2a,b.[47]

$$\Delta E = [(\Delta L)^{*2} + (\Delta a)^{*2} + (\Delta b)^{*2}]^{1/2} \qquad (3)$$

Figure S2a shows ΔE versus the amount of Cl retained in the samples. The values increased as the Cl content increased. However, the slope between the last two points, which represent ZnO-3Cl and ZnO-6Cl samples, was higher. The difference between these two points was considerably high, suggesting that the amount of Cl retained in the sample is not solely responsible for the color changes. Figure S2b shows ΔE versus the amount of Cl added to the samples. The perceptual distances from ZnO increased almost linearly with the Cl content added to the samples. Similar behavior was seen for I-doped TiO_2, in which defects were formed during iodine evaporation.[46] In this study, the data indicate that surface defects are also formed during Cl evaporation.

X-ray photoelectron spectroscopy (XPS) was utilized to examine the presence of chlorine (Cl) in the doped ZnO samples. The Cl 2p spectra for ZnO-6Cl, the ZnO-sample, are shown in Figure 2d, while those for ZnO-1Cl and ZnO-3Cl are illustrated in Figure S3a,b, respectively. Within these spectra, two distinct peaks, located at approximately 199.3 and 200.9 eV, correspond to Cl $2p_{3/2}$ and Cl $2p_{1/2}$, respectively.[48] The binding energy associated with Cl $2p_{3/2}$ indicates the formation of $ZnCl_2$, confirming the successful doping of Cl atoms into ZnO, effectively substituting oxygen (O) atoms within the lattice structure.[49] These observations also suggest that the majority of Cl is localized on the surface of the ZnO nanoparticles. However, given the inherent surface sensitivity of XPS, precise determination of the Cl distribution within the sample remains challenging.

To address this, scanning transmission electron microscopy (STEM) and energy-dispersive X-ray spectroscopy (EDS) elemental mapping was conducted on the ZnO-6Cl sample, as depicted in Figure 3.

Figure 3a shows the HAADF image of the area chosen to acquire the EDS spectrum. Figure 3b−d shows the intensity peak maps for chlorine (green), zinc (red), and oxygen (blue), respectively. Figure 3e,f shows the ratio between the Cl and Zn peak intensities and the ratio between the Cl and O peak intensities, respectively. Both Zn and O maps follow approximately the same contrast variation observed in the HAADF image; however, the O map is noisier than the Zn map. To clarify, the term "ratio" in this context refers to the intensity peak of Cl divided by the intensity peak of Zn for each pixel in Figure 3e, and the intensity peak of Cl divided by the intensity peak of O for each pixel in Figure 3f. This ratio
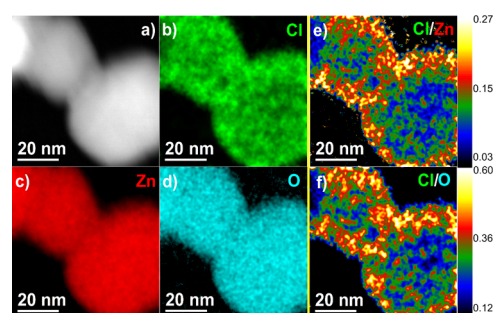

Figure 3. STEM EDS mapping of the ZnO-6Cl sample. (a) HAADF image. (b−d) intensity peak maps for chlorine (green), zinc (red), and oxygen (blue), respectively; (e) ratio between Cl and Zn peaks intensities; and (f) ratio between Cl and O peaks intensities.

cannot be straightforwardly interpreted as a compositional ratio; however, it can be correlated since the composition between elements A and B is related to the intensity ratios in the first approximation ($C_A/C_B = K_{AB} (I_A/I_B)$). To ensure reliable results, only intensities higher than 3× the background in Figure 3b−d were considered; otherwise, pixel intensity was set to 0. Additionally, to avoid division by zero during the ratio calculations, a value of 1 was added to the denominator.

The thin regions are darker in all three images (a−c), while the contrast observed in the Cl map is higher on the surface of the nanoparticle. The ratio between Cl and Zn, as presented in Figure 3e, indicates an enrichment of Cl at the edge of the nanoparticle, with a thickness of approximately 6 nm. The dark blue region in Figure 3e has an average ratio of 0.05, while the edge region, shown in yellow/red, has an average ratio of 0.20. This corresponds to a four-fold enrichment of Cl at the edge/surface. Similarly, the ratio between Cl and O, as shown in Figure 3f, also indicates an enrichment of Cl at the edge of the nanoparticle, with a thickness of approximately 6 nm. The average ratio for the dark blue region in Figure 3f is 0.15, whereas the edge region in yellow/red has an average ratio of 0.45. This represents a three-fold enrichment of Cl at the edge/surface. The difference in the average values between Figure 3e,f can be attributed to the differing ionization yields of the Zn(K) and O(K) edges. These features point to the formation of a Cl layer on the surface of ZnO-6Cl nanoparticles, which confirms the evidence seen previously. Similar dopant enrichment on the surface has been observed in other similar systems, such as BaO-doped TiO_2,[6] SrO-doped TiO_2, and MgO-doped TiO_2.[5]

The formation of zinc chloride ($ZnCl_2$) on the surface of the nanoparticles has been reported to be responsible for catalyst deactivation, a phenomenon known as chloride poisoning.[31] The ZnO surface at neutral pH (∼7) is positively charged, and soluble Cl can be strongly adsorbed, hindering the adsorption of organic reactants.[50] In the particular case of photocatalysis, adsorbed Cl sterically blocks the adsorption of organic pollutants.[32]

In this study, we intentionally removed Cl ions from the surface of ZnO nanoparticles using the selective surface lixiviation method to avoid the chloride poisoning phenomenon and improve the photocatalytic response of Cl-doped ZnO due to the improvement in the GB electrical conductivity. Our previous work showed that Cl segregated in GBs increases the electrical conductivity of ZnO nanoparticles.[34] In this study, the goal is to show how it affects the photocatalytic activity.

3.2. Selective Surface Lixiviation, DRIFTS, and EPRs.

The details of the selective surface lixiviation method are shown in Section 2. The powders collected after the treatment were used in the photocatalytic tests. The representation of ZnO nanoparticles in the bottom left corner of Figure 1 shows that, after treatment, Cl remained only in the GB and the bulk of the material. These powders were labeled lixiviated, and the suffix Lix was added to the sample labels. The ones that did not go through this process were labeled nonlixiviated.

Surface segregation of dopants is also called surface excess, and it is represented by the capital Greek letter gamma. The surface excess is denoted by Γ_{Cl}^S and was calculated using eq 4,[6,8−10,34] while the GB excess, indicated by Γ_{Cl}^{GB}, was calculated from eq 5.

$$\Gamma_{Cl}^S = \frac{n_{Cl}^S}{SSA} \quad (4)$$

$$\Gamma_{Cl}^{GB} = \frac{n_{Cl}^T - n_{Cl}^S - n_{Cl}^{bulk}}{SGB} \quad (5)$$

where n_{Cl}^T is the total amount of Cl (mol g^{-1}) in the material, and n_{Cl}^{bulk} is the Cl dissolved in the bulk (mol g^{-1}). n_{Cl}^T and n_{Cl}^S are directly measured by ISE chemical analysis, and n_{Cl}^{bulk} is estimated. Assuming the same analysis as used by Fortes et al.,[34] the bulk solubility was estimated as 0.044% Cl. The results are shown in Table 2. Most of the Cl is segregated on the surface, reaching ∼6 μmol/m^2 for the ZnO-6Cl sample. The data agree with the STEM EDS mapping observed in Figure 3.

Table 2. Surface Excess (Γ_{Cl}^S), GB Excess (Γ_{Cl}^{GB}), and $\Gamma_{Cl}^{GB}/\Gamma_{Cl}^S$ for Undoped and Cl-Doped ZnO

sample	Γ_{Cl}^S (μmol/m^2)	Γ_{Cl}^{GB} (μmol/m^2)	$\Gamma_{Cl}^{GB}/\Gamma_{Cl}^S$
ZnO	0.15 ± 0.01	0.04 ± 0.04	0.26 ± 0.27
ZnO-1Cl	2.14 ± 0.19	0.26 ± 0.06	0.12 ± 0.04
ZnO-3Cl	4.63 ± 0.41	0.87 ± 0.11	0.19 ± 0.04
ZnO-6Cl	6.32 ± 0.55	1.42 ± 0.27	0.23 ± 0.06

The characterizations presented from this point forward, including DRIFTS, TEM, EPR, EIS, and photocatalysis, were performed on nonlixiviated and lixiviated powders. Diffuse reflectance infrared Fourier-transform (DRIFT) spectroscopy was the first analysis performed. The results are presented in Figure 4. Figure 4a shows the DRIFTS results for the undoped ZnO nanoparticles, and Figure 4b shows the results for the ZnO-6Cl sample. In both cases, solid lines denote the nonlixiviated samples, and dot lines represent the lixiviated samples. The peaks ranging from 800 to 1200 cm^{-1} are characteristic of Zn−O surface vibrations and phonon mode vibrations (700−1100 cm^{-1}) of ZnO.[51] The 1414 and 1507 cm^{-1} peaks are observed in all samples and can be attributed to carbonates,[52] adsorbed CO$_2$,[53,54] surface Zn−OH groups,[54] or even adsorbed H$_2$O.[54] For undoped ZnO, these peaks increased after lixiviation. The wide band from ∼2700 to ∼3700 cm^{-1} is associated with adsorbed water and OH vibrations and is seen in all compositions.[54,55] This broadband is typical of oxide nanoparticles and is related to the capacity to adsorb H$_2$O and the high SSA of the nanoparticles. The two peaks at 3448 and 3497 cm^{-1} are seen only in the ZnO-6Cl sample and are assigned to the free O−H stretching vibrations from adsorbed hydroxyl groups characteristic of the ZnCl$_2$
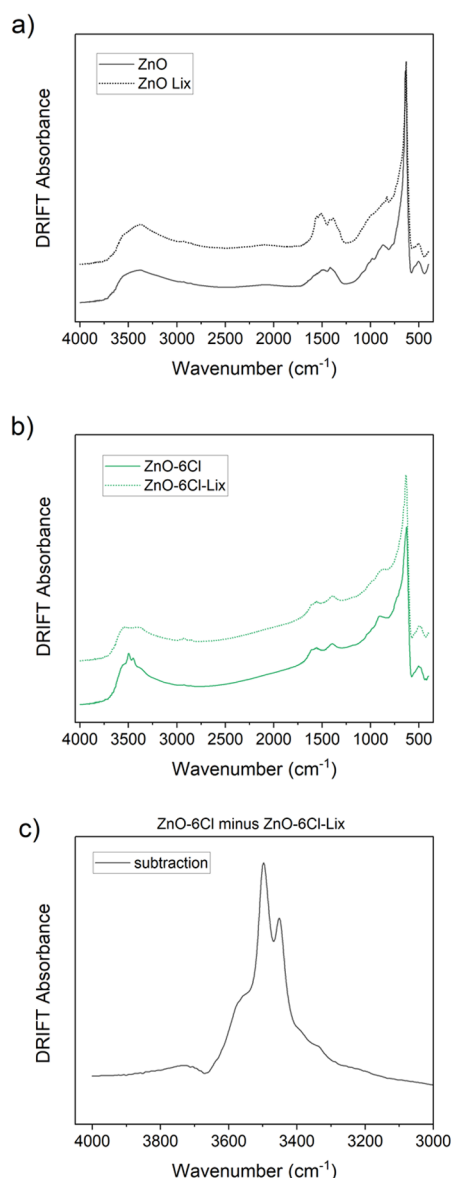

Figure 4. DRIFTS spectra for (a) undoped ZnO nanoparticles, (b) Cl-doped ZnO samples, and (c) spectral difference between the nonlixiviated and the lixiviated samples. Dot lines represent the lixiviated samples, and solid lines represent the nonlixiviated samples.

surface.[56] This result agrees with the XPS results, which confirm the formation of ZnCl$_2$ on the surfaces of ZnO-doped samples. The absence of these peaks in the ZnO-6Cl-Lix sample indicates that the chloride was successfully removed from the surface. Removal of these peaks is more clearly evidenced in Figure 4c: subtraction of ZnO-6Cl and ZnO-6Cl-Lix clearly shows the species related to the surface of ZnCl$_2$.

Figure S5 shows the TEM images and particle size distribution histograms for pure ZnO, Cl-doped ZnO (ZnO-6Cl), and lixiviated Cl-doped ZnO (ZnO-6Cl-Lix) samples. The TEM images do not show any clear differences between the undoped and doped samples or between the unlixiviated and the lixiviated samples. The particle size distributions also show similar average particle sizes: 32 ± 11 nm for pure ZnO, 33 ± 10 nm for ZnO-6Cl, and 29 ± 10 nm for ZnO-6Cl-Lix. On average, the mean particle sizes for lixiviated samples decreased slightly, which might be due to the slight solubility
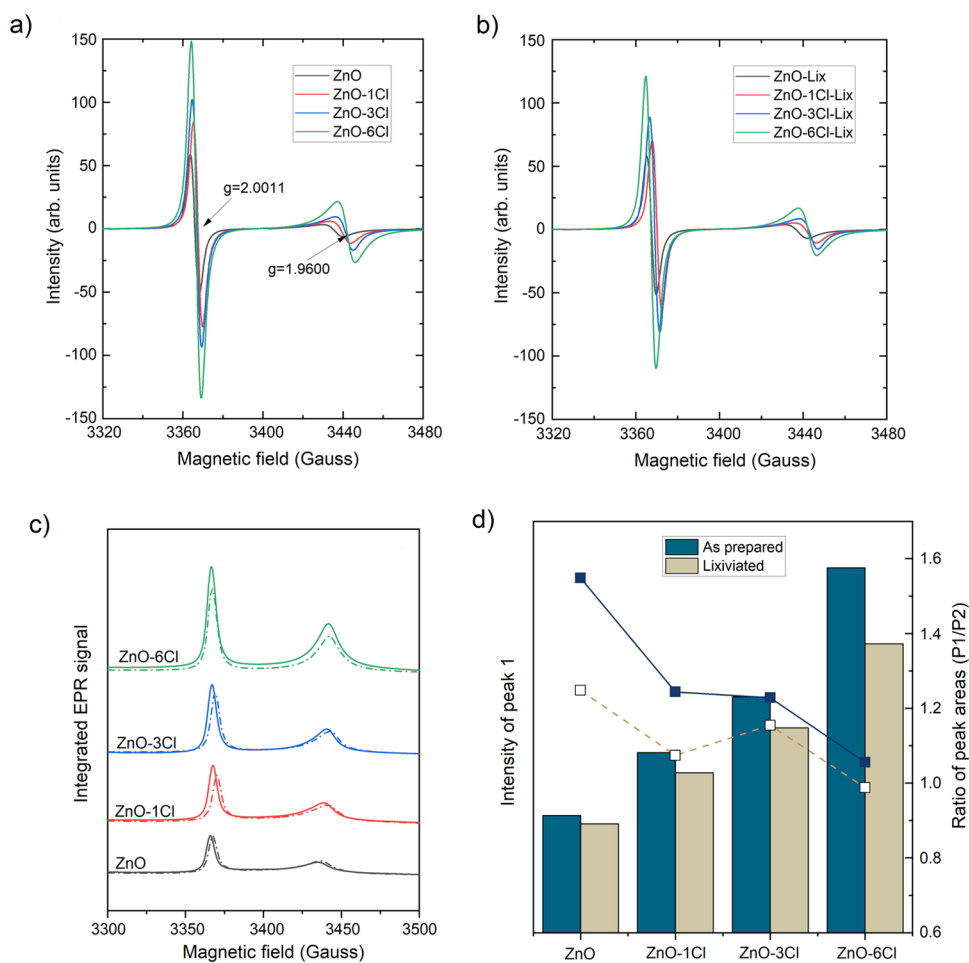
Figure 5. Room-temperature EPR spectra of the ZnO samples. EPR signals of ZnO (a) as prepared and (b) after the lixiviation process; (c) their respective absorption spectra, and (d) inspection of the area of the peaks corresponding to $g = 1.9600$ (bar graph) and the ratio of peak areas (scatter-line) for the as-prepared and lixiviated ZnO samples.

of ZnO in water (0.2−0.5 mg/L) at pH 7.0. The same behavior was noticed in the average crystallite sizes calculated by Rietveld refinement (Table S1). However, both results are still within the standard deviation, suggesting that the doping and lixiviation processes did not have a significant effect on ZnO nanoparticle sizes. Additional TEM images are provided in Figure S6.

The paramagnetic response of undoped ZnO and Cl-doped ZnO samples was assessed by using EPR. The results are shown in Figures 5 and S7. Figure 5a shows the EPR spectra of all samples obtained at room temperature for nonlixiviated samples, while Figure 5b displays the spectra for lixiviated samples. The spectra show two distinct features, at g-factors near 1.9600 and 2.0011, which are usually assigned to shallow donor states caused by surface oxygen vacancies (V_O^+) or interstitial Zn atoms (Zn_i), and to Zn vacancies (V_{Zn}), respectively.[57] In nanosized materials, these features are explained in terms of the core−shell model, according to which, the signal at 1.9600 relates to bulk or GB-segregated defects, and the signal at 2.0011 corresponds to surface levels.[58,59] The effect of Cl on the intensity of both signals is clear. Inspection of the absorption spectra, given by the first integral of the EPR signal, makes this distinction clearer (Figure 5c). The increasing presence of Cl ions increased both EPR signals.

Furthermore, lixiviation did not appear to affect the trend of the signals concerning the increase in Cl dopants. Nevertheless, the position of the peaks (hence the g-factor) shows a shift toward higher values of the magnetic field.

Figure S7 shows the results of the analysis carried out at 100 K. For all samples analyzed, the magnitudes of the signal of the first peak do not show appreciable differences compared to the spectra obtained at room temperature. However, the second peak signal ($g = 1.9600$) is significantly stronger at 100 K. Furthermore, the spectra of the undoped sample and the sample with the lesser amount of added dopant exhibit a small feature near $g = 1.9845$. However, this feature gradually disappears when more Cl is added to the system.

Inspection of the absorption spectra reveals a curious pattern: the signals for the undoped samples intensify after the lixiviation process, whereas the doped samples generally exhibit a slight decrease in intensity. Notably, the exception to this trend is the material with the greatest dopant concentration (ZnO-6Cl), which exhibits peak intensities that remain constant regardless of the lixiviation process.

The area of the absorption peaks is proportional to the concentration of the species present in the sample. Figures 5d and S7d show the trend of areas of the peak corresponding to $g = 1.9600$ (peak 1) for nonlixiviated and lixiviated samples, respectively, along with the trend of the peak ratios ($g = 1.9600$ by $g = 2.0011$). It can be seen that an increase in Cl content

will generally increase the presence of paramagnetic species in the material (possibly V_O). Moreover, the trend is not affected by washing the surface-segregated Cl, although the energy absorption is reduced more significantly in the lixiviated samples.

Additionally, the ratio of the signals of both features, P1/P2, shows that the distribution of defects is considerably affected by the addition of Cl into the material. While increasing the amount of Cl appears to favor the formation of both defects at g = 1.9600 (P2) and 2.0011 (P1), the formation/stabilization of defects at g = 1.9600 at room temperature is more pronounced, gradually reducing the ratio P1/P2 to near 1.0 under this condition. Conversely, at 100 K, the trend is reversed, and Cl seems to promote the formation/stabilization of defects at g = 2.0011. This comparison suggests that the bulk/GB defects (g = 1.9600) are stabilized by the incorporation of Cl ions in these locations, as a consequence of the increasing Γ_{Cl}^{GB} observed in the samples. However, because these defects are more mobile than surface-segregated defects, increasing temperature tends to quench them to some extent, lowering their EPR signals. Surface-segregated defects, on the other hand, are more strongly localized, and hence are more stable to temperature changes. Therefore, an inspection of the spectra obtained at 100 K will likely provide more relevant information about the defect structure of the material.

An analysis of the P1/P2 ratio (surface/bulk+GB defects) indicates that increasing the amount of Cl increases the number of surface defects and the proportion of surface-to-bulk/GB defects. When the samples are lixiviated, the ratio seems to stabilize at ∼0.52, suggesting that there are twice as many defects in the bulk/GB than at the surface of the doped oxides.

3.3. Electrical Measurements and Photocatalytic Reactions.

The electrical measurements of the samples were performed by electrochemical impedance spectroscopy. The main objective was to access the electrical transport properties of the samples, especially through the grain boundaries. The results are shown in Figure 6a,b, which represent nonlixiviated

Figure 6. Impedance spectroscopy diagrams for nonlixiviated (a) and lixiviated (b) Cl-doped ZnO pellets measured at 150 °C. The numbers indicate the logarithm of the frequency. The ZnO data is divided by a factor of 10 to fit the displayed scale.

and lixiviated samples, respectively. The nanopowders used in these measurements were pressed pellets with similar relative densities (46−50 vol %). The first data obtained from the measurements were the total electrical conductivity, which was extracted from the EIS spectra at 150 °C. The data were acquired from the low-frequency end of the EIS diagram interception with the real axis. The results were 4.14×10^{-6}, 6.11×10^{-5}, 6.73×10^{-4}, and 2.22×10^{-4} $\Omega^{-1} \cdot cm^{-1}$, which correspond to the ZnO, ZnO-1Cl, ZnO-3Cl, and ZnO-6Cl samples, respectively. An increment in the total electrical conductivity is observed with the increase in Cl doping. The dopant promoted an increment of 2 orders of magnitude, which follows the increase in surface and GB excesses shown in Table 2.

The IS diagrams shown in Figure 6 present at least two semicircles, corresponding to different electrical contributions, which can be associated with several transport phenomena, such as bulk transport, space charge layers, surface ionic diffusion, blocking of charge carriers in pores, and electrode reactions.[17,60,61]

The EIS data of the lixiviated samples (Figure 6b) presented a trend similar to that observed for the nonlixiviated samples. However, a more pronounced decrease in electrical resistivity was observed for Cl-doped samples. A remarkable correlation is seen between the amount of Cl and the total electrical conductivity; the higher the Cl doping, the higher the electrical conductivity.

The last analysis performed on ZnO and Cl-doped ZnO samples was the photocatalytic activity. The experiments were performed on nonlixiviated and lixiviated samples to obtain insight into the role of Cl-doping ZnO. Previous studies have shown that soluble Cl can inhibit photocatalytic reactions.[31,32,50] The Cl segregated on the surface of ZnO nanopowders is susceptible to solubilization in water during photocatalysis, causing significant interference in the photocatalytic reaction. However, we hypothesize that if the Cl from the ZnO surface is removed before the photocatalytic reaction, the photoactivity might be improved due to the decrease in the electrical barrier at the GB, which also affects the electrical conductivity.

The electrical conductivity is affected by the doping ion and can be modulated, depending on where it is segregated, as discussed previously. The improvement in electrical conductivity promoted by Cl excess in the GB can increase the mean free path of the photogenerated charge carriers (e⁻ and h⁺) and extend their lifetimes, which are essential for the degradation of ACT.[62] Both contributions are expected to change the efficiency of the photocatalytic performance.

Acetaminophen (ACT) was selected as the tracer to evaluate the effects of doping and lixiviation on the photocatalytic performance of ZnO. Figure 7a shows the degradation profile of ACT after the reaction for nonlixiviated Cl-doped ZnO samples. The results are normalized by the surface area of the samples. The efficiency of the photocatalytic reaction, measured at 180 min of exposure to UV irradiation, increases for low concentrations of dopants, that is, samples ZnO-1Cl and ZnO-3Cl, but decreases for higher concentrations (ZnO-6Cl). As presented in Table 2, surface and GB segregation increase with total Cl concentration, but at low concentrations, the increase in electrical conductivity seems to be predominant against the deleterious effects of soluble Cl from ZnO surfaces. However, the high amount of soluble Cl from the surface of
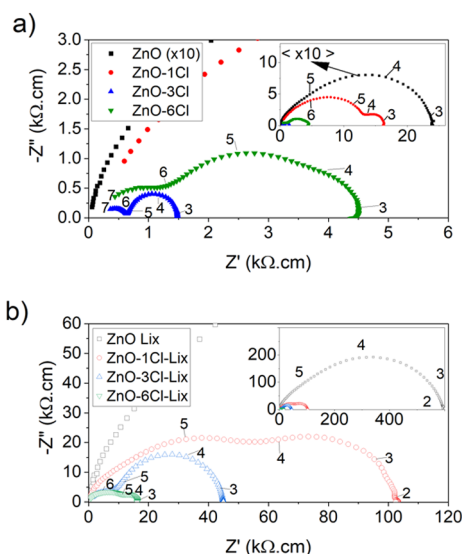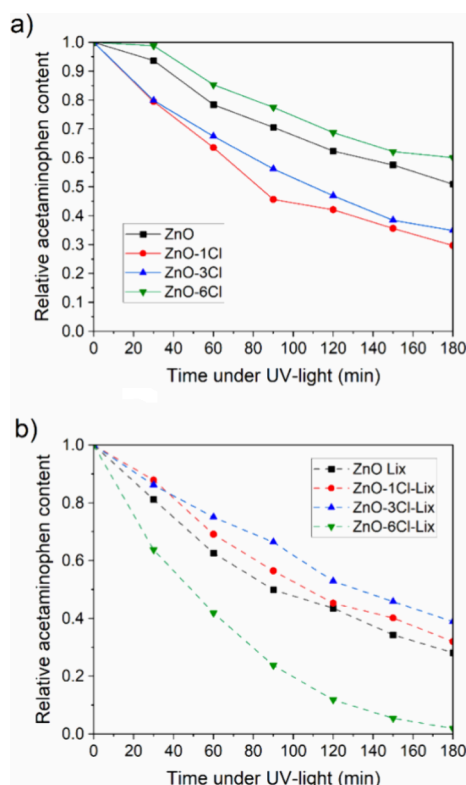
Figure 7. ACT photodegradation of nonlixiviated (a) and lixiviated (b) Cl-doped ZnO, upon irradiation of 4.1 mW/cm^2 of a monochromatic UV-A light (370 nm).

the ZnO-6Cl sample makes this sample the least effective of the series.

New photocatalysis assays were performed using the lixiviated samples to demonstrate that the balance between the Cl segregated in the GB and the elimination of the soluble Cl segregated on the surface can improve photocatalysis by promoting more efficient charge-carrier transport in the absence of detrimental surface-segregated species. Figure 7b presents the ACT photodegradation results, which show a modification in the photocatalytic efficiency; the most efficient sample was that containing the greatest amount of Cl segregated in the GB (ZnO-6Cl-Lix) and, consequently, the highest electrical conductivity. An improvement in ACT photodegradation after lixiviation was also observed for undoped ZnO, which can be associated with the removal of Cl from the surface as well as the surface modification due to the lixiviation process. Figure S8 illustrates the relationship between ACT conversion and the Cl excess partition between the GB and the surface.

The photocatalysis kinetics and efficiency parameters are summarized in Table S2. It can be seen that lixiviation substantially improves the performance of ZnO-6Cl, reaching a reaction rate of 19.5×10^{-3} min^{-1}. The results are comparable to previously reported data on ACT degradation by ZnO under simulated solar irradiation, which showed reaction rates ranging from 3.8 to 52.4×10^{-3} min^{-1} for N-doped ZnO[63] and by a ZnO/g-C$_3$N$_4$ heterojunction,[64] respectively. Additionally, the performance is comparable to the standard P25 TiO$_2$, which has a reported rate of 2.5×10^{-3} min^{-1}.[65]

The results demonstrate that Cl segregation at the nano-ZnO interfaces plays a crucial role in photocatalytic processes. These results reinforce the importance of the often-neglected

charge-carrier transport properties in the design of efficient catalysts. Moreover, the results confirm that the selective lixiviation method is a powerful tool to improve photocatalytic processes.

4. CONCLUSIONS

In summary, this study demonstrated the effectiveness of the selective lixiviation method in enhancing the performance of Cl-doped ZnO nanoparticles for the target application of acetanomiphen degradation. Interface segregation of Cl on nano-ZnO was observed at both the surface and grain boundaries, with no discernible dependence of band gap energy on Cl concentration. STEM EDS elemental mapping revealed a Cl-enriched layer at the periphery of the ZnO nanoparticles, approximately 6 nm thick. These findings underscore the significance of controlling dopant distribution to optimize nanoparticle properties. The selective lixiviation approach proves efficient in achieving this control. The Cl-doped ZnO nanoparticles investigated in this study serve as a valuable reference for future research involving different systems, offering insights into the manipulation of dopant distribution for enhanced functionality.

■ ASSOCIATED CONTENT

ⓢ Supporting Information

The Supporting Information is available free of charge at https://pubs.acs.org/doi/10.1021/acsanm.4c06747.

Bandgap energies of ZnO and Cl-doped ZnO samples calculated using the Tauc model; relationship between ΔE and the amount of Cl retained or added in the samples; XPS spectra of Cl 2p for ZnO-1Cl and ZnO-3Cl samples; SEM images of zinc oxide nanoparticles (pure ZnO, ZnO-6Cl, and ZnO-6Cl-Lix) highlighting surface morphology; TEM images and particle size distribution histograms of ZnO and Cl-doped ZnO samples (pure ZnO, ZnO-6Cl, and ZnO-6Cl-Lix); EPR spectra of ZnO samples obtained at 100 K before and after lixiviation, including bar graphs and scatter-line plots of peak areas; effect of grain boundary (GB) to surface Cl excess on photocatalytic removal of ACT; total Cl content, crystallite size, and SSA of lixiviated ZnO and Cl-doped ZnO samples; and photocatalysis results, including ACT conversion after 180 min (X180) and the pseudo-first-order reaction rate constant (k) (PDF)

■ AUTHOR INFORMATION

Corresponding Author

Andre Luiz da Silva − *Department of Metallurgical and Materials Engineering, Polytechnic School − University of São Paulo, BR-05508030 São Paulo, Brazil;* ⓞ orcid.org/0000-0001-8006-8870; Phone: +55 11 3091 6087; Email: andresilva.urussanga@usp.br

Authors

Gustavo M. Fortes − *Department of Metallurgical and Materials Engineering, Polytechnic School − University of São Paulo, BR-05508030 São Paulo, Brazil;* ⓞ orcid.org/0000-0001-7366-8675

Bruno Ramos − *Department of Metallurgical and Materials Engineering, Polytechnic School − University of São Paulo, BR-05508030 São Paulo, Brazil; Microfluidic and*

Photoelectrocatalytic Engineering Lab. Department of Chemical Engineering, FEI University Centre, BR-09850901 São Bernardo do Campo, Brazil; orcid.org/0000-0003-1932-6046

Jefferson Bettini − *Brazilian Nanotechnology National Laboratory (LNNano), BR-13083100 Campinas, Brazil*

Fabio Coral Fonseca − *IPEN-CNEN/SP, Instituto de Pesquisas Energéticas e Nucleares, BR-05508000 São Paulo, Brazil;* orcid.org/0000-0003-0708-2021

Renato V. Gonçalves − *São Carlos Institute of Physics, University of São Paulo, BR-13560970 São Carlos, Brazil;* orcid.org/0000-0002-3372-6647

Orlando Rodrigues Junior − *IPEN-CNEN/SP, Instituto de Pesquisas Energéticas e Nucleares, BR-05508000 São Paulo, Brazil;* orcid.org/0000-0002-6704-1910

Douglas Gouvea − *Department of Metallurgical and Materials Engineering, Polytechnic School − University of São Paulo, BR-05508030 São Paulo, Brazil;* orcid.org/0000-0003-3607-8793

Complete contact information is available at:
https://pubs.acs.org/10.1021/acsanm.4c06747

Notes

The authors declare no competing financial interest.

ACKNOWLEDGMENTS

REFERENCES

(1) Chaudhary, R. G.; Sonkusare, V.; Bhusari, G.; Mondal, A.; Potbhare, A.; Juneja, H.; Abdala, A.; Sharma, R. Preparation of Mesoporous ThO2 Nanoparticles: Influence of Calcination on Morphology and Visible-Light-Driven Photocatalytic Degradation of Indigo Carmine and Methylene Blue. *Environ. Res.* **2023**, *222*, No. 115363.

(2) Ma, Z.; Li, Y.; Lv, Y.; Sa, R.; Li, Q.; Wu, K. Synergistic Effect of Doping and Compositing on Photocatalytic Efficiency: A Case Study of La2Ti2O7. *ACS Appl. Mater. Interfaces* **2018**, *10* (45), 39327− 39335.

(3) Qin, H.; Li, W.; Xia, Y.; He, T. Photocatalytic Activity of Heterostructures Based on ZnO and N-Doped ZnO. *ACS Appl. Mater. Interfaces* **2011**, *3* (8), 3152−3156.

(4) Chen, Q.; Gao, G.; Fan, H.; Zheng, J.; Ma, L.; Ding, Y.; Fang, Y.; Duan, R.; Cao, X.; Guo, Y.; Ma, D.; Hu, X. Synergy of Oxygen Vacancies and Acid Sites on N-Doped WO3 Nanobelts for Efficient C−C Coupling Synthesis of Benzoin Isopropyl Ether. *ACS Appl. Mater. Interfaces* **2022**, *14* (3), 4725−4738.

(5) da Silva, A. L.; Bettini, J.; Bernardes, A. A.; Castro, R. H. R.; Gouvêa, D. Improving TiO2 Anatase Nanostability Via Interface Segregation: The Role of the Ionic Radius. *J. Phys. Chem. C* **2023**, *127* (3), 1536−1547.

(6) da Silva, A. L.; Muche, D. N. F.; Caliman, L. B.; Bettini, J.; Castro, R. H. R.; Navrotsky, A.; Gouvêa, D. TiO 2 Surface Engineering to Improve Nanostability: The Role of Interface Segregation. *J. Phys. Chem. C* **2019**, *123* (8), 4949−4960.

(7) Gandelman, H.; da Silva, A. L.; Ramos, B.; Gouvêa, D. Interface Excess on Sb-Doped TiO2 Photocatalysts and Its Influence on Photocatalytic Activity. *Ceram. Int.* **2021**, *47* (1), 619−625.

(8) Gandelman, H.; da Silva, A. L.; Caliman, L. B.; Gouvêa, D. Surface and Grain Boundary Excess of ZnO-Doped TiO2 Anatase Nanopowders. *Ceram. Int.* **2018**, *44* (10), 11390−11396.

(9) Bernardes, A. A.; Caliman, L. B.; da Silva, A. L.; Bettini, J.; Guimarães, K. L.; Gouvea, D. Li < inf > 2</Inf > O-Doped MgAl < inf > 2</Inf > O < inf > 4</Inf> Nanopowders: Energetics of Interface Segregation. *J. Am. Ceram. Soc.* **2020**, *103* (4), 2835−2844.

(10) Da Silva, A. L.; Wu, L.; Caliman, L. B.; Castro, R. H. R.; Navrotsky, A.; Gouvêa, D. Energetics of CO2and H2O Adsorption on Alkaline Earth Metal Doped TiO2. *Phys. Chem. Chem. Phys.* **2020**, *22* (27), 15600−15607.

(11) de Oliveira, R. A. M. P.; da Silva, A. L.; Caliman, L. B.; Gouvêa, D. Interface Excess on Li2O-Doped γ-Al2O3 Nanoparticles. *Ceram. Int.* **2020**, *46* (8), 10555−10560.

(12) Caliman, L. B.; da Silva, A. L.; Gouvêa, D. Self-segregation and Solubility in Nonstoichiometric MgAl 2 O 4 Nanoparticles. *J. Am. Ceram. Soc.* **2022**, *105* (7), 4994−5002.

(13) Muche, D. N. F.; da Silva, A. L.; Nakajima, K.; Gouvêa, D.; Castro, R. H. R. Simultaneous Segregation of Lanthanum to Surfaces and Grain Boundaries in MgAl2O4 Nanocrystals. *Appl. Surf. Sci.* **2020**, *529*, No. 147145.

(14) Neves, D. C. O. S.; da Silva, A. L.; de Oliveira Romano, R. C.; Gouvêa, D. Fe2O3-Doped SnO2Membranes with Enhanced Mechanical Resistance for Ultrafiltration Application. *J. Eur. Ceram Soc.* **2020**, *40* (15), 5959−5966.

(15) Castro, R. H. R.; Ushakov, S. V.; Gengembre, L.; Gouvêa, D.; Navrotsky, A. Surface Energy and Thermodynamic Stability of γ-Alumina: Effect of Dopants and Water. *Chem. Mater.* **2006**, *18* (7), 1867−1872.

(16) Simpson, J. C.; Cordaro, J. F. Characterization of Deep Levels in Zinc Oxide. *J. Appl. Phys.* **1988**, *63* (5), 1781−1783.

(17) Lee, J.; Hwang, J.-H.; Mashek, J. J.; Mason, T. O.; Miller, A. E.; Siegel, R. W. Impedance Spectroscopy of Grain Boundaries in Nanophase ZnO. *J. Mater. Res.* **1995**, *10* (9), 2295−2300.

(18) Özgür, Ü.; Alivov Ya, I.; Liu, C.; Teke, A.; Reshchikov, M. A.; Doğan, S.; Avrutin, V.; Cho, S.-J.; Morkoç, H. A Comprehensive Review of ZnO Materials and Devices. *J. Appl. Phys.* **2005**, *98* (4), No. 041301.

(19) Wöll, C. The Chemistry and Physics of Zinc Oxide Surfaces. *Prog. Surf. Sci.* **2007**, *82*, 55−120.

(20) Li, Z.; Li, J.; Xiong, M.; Lei, J.; Chen, Y.; Zhang, S. Effects of Mo Single-Doping and Mo-Al Co-Doping on ZnO Transparent Conductive Films. *Appl. Surf. Sci.* **2022**, *584*, No. 152588.

(21) Yildiz, A.; Kayhan, B.; Yurduguzel, B.; Rambu, A. P.; Iacomi, F.; Simon, S. Ni Doping Effect on Electrical Conductivity of ZnO Nanocrystalline Thin Films. *Journal of Materials Science: Materials in Electronics* **2011**, *22* (9), 1473−1478.

(22) Serin, T.; Uzun, Ş.; Çam, E.; Serin, N.; Yildiz, A. Electrical Conduction Properties of In-Doped ZnO Thin Films. *Phys. Scr.* **2011**, *84* (6), No. 065703.

(23) Yildiz, A.; Yurduguzel, B.; Kayhan, B.; Calin, G.; Dobromir, M.; Iacomi, F. Electrical Conduction Properties of Co-Doped ZnO Nanocrystalline Thin Films. *Journal of Materials Science: Materials in Electronics* **2012**, *23* (2), 425−430.

(24) Tsay, C. Y.; Cheng, H. C.; Tung, Y. T.; Tuan, W. H.; Lin, C. K. Effect of Sn-Doped on Microstructural and Optical Properties of ZnO Thin Films Deposited by Sol-Gel Method. *Thin Solid Films* **2008**, *517* (3), 1032−1036.

(25) Yousefi, R.; Jamali-Sheini, F. Effect of Chlorine Ion Concentration on Morphology and Optical Properties of Cl-Doped ZnO Nanostructures. *Ceram. Int.* **2012**, *38* (7), 5821−5825.

(26) Jiamprasertboon, A.; Powell, M. J.; Dixon, S. C.; Quesada-Cabrera, R.; Alotaibi, A. M.; Lu, Y.; Zhuang, A.; Sathasivam, S.; Siritanon, T.; Parkin, I. P.; Carmalt, C. J. Photocatalytic and Electrically Conductive Transparent Cl-Doped ZnO Thin Films: Via Aerosol-Assisted Chemical Vapour Deposition. *J. Mater. Chem. A Mater.* **2018**, *6* (26), 12682−12692.

(27) Wang, F.; Seo, J. H.; Li, Z.; Kvit, A. V.; Ma, Z.; Wang, X. Cl-Doped ZnO Nanowires with Metallic Conductivity and Their Application for High-Performance Photoelectrochemical Electrodes. *ACS Appl. Mater. Interfaces* **2014**, *6* (2), 1288−1293.

(28) Liu, C.; Yu, A.; Peng, M.; Song, M.; Liu, W.; Zhang, Y.; Zhai, J. Improvement in the Piezoelectric Performance of a ZnO Nano-generator by a Combination of Chemical Doping and Interfacial Modification. *J. Phys. Chem. C* **2016**, *120* (13), 6971−6977.

(29) Zhang, Y.; Liu, C.; Liu, J.; Xiong, J.; Liu, J.; Zhang, K.; Liu, Y.; Peng, M.; Yu, A.; Zhang, A.; Zhang, Y.; Wang, Z.; Zhai, J.; Wang, Z. L. Lattice Strain Induced Remarkable Enhancement in Piezoelectric Performance of ZnO-Based Flexible Nanogenerators. *ACS Appl. Mater. Interfaces* **2016**, *8* (2), 1381−1387.

(30) Gordon, R. G. Criteria for Choosing Transparent Conductors. *MRS Bull.* **2000**, *25* (8), 52−57.

(31) Ray, N.; Rastogi, V. K.; Chhabra, D. S.; Dutt, S.; Sen, S. P. *DEACTIVATION OF LOW TEMPERATURE SHIFT CATALYST Part II Poisoning by Chlorine*, 1982; Vol. *30*.

(32) Krivec, M.; Dillert, R.; Bahnemann, D. W.; Mehle, A.; Štrancar, J.; Dražić, G. The Nature of Chlorine-Inhibition of Photocatalytic Degradation of Dichloroacetic Acid in a TiO2-Based Microreactor. *Phys. Chem. Chem. Phys.* **2014**, *16*, 14867−14873.

(33) Lessing, P. A. Mixed-Cation Oxide Powders via Polymeric Precursors. *Am. Ceram. Soc. Bull.* **1989**, *68*, 1002−1007.

(34) Fortes, G. M.; da Silva, A. L.; Caliman, L. B.; Fonseca, F. C.; Gouvêa, D. Interfacial Segregation in Cl−-Doped Nano-ZnO Polycrystalline Semiconductors and Its Effect on Electrical Properties. *Ceram. Int.* **2021**, *47*, 24860−24867.

(35) da Silva, A. L.; Trindade, F. J.; Dalmasso, J. Lou; Ramos, B.; Teixeira, A. C. S. C.; Gouvêa, D. Synthesis of TiO2Microspheres by Ultrasonic Spray Pyrolysis and Photocatalytic Activity Evaluation. *Ceram. Int.* **2022**, *48* (7), 9739−9745.

(36) Castro, R. H. R.; Gouvêa, D. Sintering and Nanostability: The Thermodynamic Perspective. *J. Am. Ceram. Soc.* **2016**, *99* (4), 1105−1121.

(37) Searcy, A. W.; Bullard, J. W. Thermodynamics and Kinetics of Surface Area Changes of Faceted Particles. *J. Am. Ceram. Soc.* **1994**, *77* (9), 2314−2318.

(38) Gouvêa, D.; Do Rosário, D. C. C.; Caliman, L. B. Surface and Grain-Boundary Excess of ZnO-Doped SnO2nanopowders by the Selective Lixiviation Method. *J. Am. Ceram. Soc.* **2017**, *100* (9), 4331−4340.

(39) Kirchheim, R. Reducing Grain Boundary, Dislocation Line and Vacancy Formation Energies by Solute Segregation. II. Experimental Evidence and Consequences. *Acta Mater.* **2007**, *55* (15), 5139−5148.

(40) Wu, L.; Dey, S.; Gong, M.; Liu, F.; Castro, R. H. R. Surface Segregation on Manganese Doped Ceria Nanoparticles and Relationship with Nanostability. *J. Phys. Chem. C* **2014**, *118* (51), 30187−30196.

(41) Fernandes, M. H.; Ramos, B.; da Silva, A. L.; Gouvêa, D. Chloride-Doped ZnO Thin Films Prepared by Spray Pyrolysis: Effects on Microstructural, Optical, and Photocatalytic Properties. *Micro Nanostruct.* **2023**, *177*, No. 207550.

(42) Renaud, A.; Cario, L.; Rocquelfelte, X.; Deniard, P.; Gautron, E.; Faulques, E.; Das, T.; Cheviré, F.; Tessier, F.; Jobic, S. Unravelling the Origin of the Giant Zn Deficiency in Wurtzite Type ZnO Nanoparticles. *Sci. Rep* **2015**, *5*, No. 12914.

(43) Machado, M.; da Silva, A. L.; Moraes, L. P. R.; Rodrigues, L. N.; Caliman, L. B.; Gouvêa, D.; Fonseca, F. C. Interface Segregation of Iron Sintering Aid in Gadolinium-Doped Ceria. *CrystEngComm* **2023**, *25* (43), 6102−6110.

(44) Bernardes, A. A.; da Silva, A. L.; Bettini, J.; Freitas, J. C. C.; Castro, R. H. R.; Gouvêa, D. Solid-State NMR for the Analysis of Interface Excesses in Li-Doped MgAl2O4 Nanocrystals. *J. Am. Ceram. Soc.* **2024**, *107* (2), 1334−1347.

(45) Makuła, P.; Pacia, M.; Macyk, W. How To Correctly Determine the Band Gap Energy of Modified Semiconductor Photocatalysts Based on UV-Vis Spectra. *J. Phys. Chem. Lett.* **2018**, *9*, 6814−6817.

(46) Bernardes, A. A.; da Silva, A. L.; Ramos, B.; Fonseca, F. C.; Gouvêa, D. Intrinsic Defects Generated by Iodine during TiO2 Crystallization and Its Relationship with Electrical Conductivity and Photoactivity. *International Journal of Ceramic Engineering & Science* **2023**, *5* (5), No. e10186.

(47) Waters, M. J.; Walker, J. M.; Nelson, C. T.; Joester, D.; Rondinelli, J. M. Exploiting Colorimetry for Fidelity in Data Visualization. *Chem. Mater.* **2020**, *32* (13), 5455−5460.

(48) He, J.; Hu, J.; Mo, X.; Hao, Q.; Fan, Z.; He, G.; Wang, Y.; Li, W.; He, Q. Novel Photocatalyst Nitrogen-Doped Simonkolleite Zn5(OH)8Cl2·H2O with Vis-up-Conversion Photoluminescence and Effective Visible-Light Photocatalysis. *Appl. Phys. A* **2019**, *125* (1), 3.

(49) Boruah, B. D.; Majji, S. N.; Misra, A. Surface Photo-Charge Effect in Doped-ZnO Nanorods for High-Performance Self-Powered Ultraviolet Photodetectors. *Nanoscale* **2017**, *9* (13), 4536−4543.

(50) Piscopo, A.; Robert, D.; Weber, J. V. Influence of PH and Chloride Anion on the Photocatalytic Degradation of Organic Compounds Part I. Effect on the Benzamide and Para-Hydrox-ybenzoic Acid in TiO 2 Aqueous Solution. *Appl. Catal., B* **2001**, *35*, 117−124.

(51) Boccuzzi, F.; Morterra, C.; Scala, R.; Zecchina, A. Infrared Spectrum of Microcrystalline Zinc Oxide. Electronic and Vibrational Contributions under Different Temperature and Environmental Conditions. *Journal of the Chemical Society, Faraday Transactions 2: Molecular and Chemical Physics* **1981**, *77* (11), 2059−2066.

(52) Boccuzzi, F.; Borello, E.; Chiorino, A.; Zecchina, A. IR Detection of Surface Microscopic Modes of Microcrystalline ZnO. *Chem. Phys. Lett.* **1979**, *61* (3), 617−619.

(53) Saussey, J.; Lavalley, J.-C.; Bovet, C. Infrared Study of CO2 Adsorption on ZnO. Adsorption Sites. *Journal of the Chemical Society, Faraday Transactions 1: Physical Chemistry in Condensed Phases* **1982**, *78* (5), 1457−1463.

(54) Keyes, B. M.; Gedvilas, L. M.; Li, X.; Coutts, T. J. Infrared Spectroscopy of Polycrystalline ZnO and ZnO:N Thin Films. *J. Cryst. Growth* **2005**, *281* (2), 297−302.

(55) Atherton, K.; Newbold, G.; Hockey, J. A. Infra-Red Spectroscopic Studies of Zinc Oxide Surfaces. *Discuss. Faraday Soc.* **1971**, *52* (0), 33−43.

(56) Behloul, H.; Ferkous, H.; Bougdah, N.; Djellali, S.; Alam, M.; Djilani, C.; Sedik, A.; Lerari, D.; Jeon, B.-H.; Benguerba, Y. New Insights on the Adsorption of CI-Reactive Red 141 Dye Using Activated Carbon Prepared from the ZnCl2-Treated Waste Cotton Fibers: Statistical Physics, DFT, COSMO-RS, and AIM Studies. *J. Mol. Liq.* **2022**, *364*, No. 119956.

(57) Papari, G. P.; Silvestri, B.; Vitiello, G.; De Stefano, L.; Rea, I.; Luciani, G.; Aronne, A.; Andreone, A. Morphological, Structural, and Charge Transfer Properties of F-Doped ZnO: A Spectroscopic Investigation. *J. Phys. Chem. C* **2017**, *121* (29), 16012−16020.

(58) Jakes, P.; Erdem, E. Finite Size Effects in ZnO Nanoparticles: An Electron Paramagnetic Resonance (EPR) Analysis. *Physica Status Solidi - Rapid Research Letters* **2011**, *5*, 56−58.

(59) Kaftelen, H.; Ocakoglu, K.; Thomann, R.; Tu, S.; Weber, S.; Erdem, E. EPR and Photoluminescence Spectroscopy Studies on the Defect Structure of ZnO Nanocrystals. *Phys. Rev. B* **2012**, *86* (1), No. 014113.

(60) Fonseca, F. C.; Souza, J. A.; Jardim, R. F.; Muccillo, R.; Muccillo, E. N. S.; Gouvêa, D.; Jung, M. H.; Lacerda, A. H. Transport Properties of La0.6Y0.1Ca0.3MnO3 Compounds with Different Interfaces. *J. Eur. Ceram. Soc.* **2004**, *24* (6), 1271−1275.

(61) Fonseca, F. C.; Muccillo, R. Impedance Spectroscopy Analysis of Percolation in (Yttria-Stabilized Zirconia)-Yttria Ceramic Composites. *Solid State Ion* **2004**, *166* (1−2), 157−165.

(62) Chau, J. H. F.; Lai, C. W.; Leo, B. F.; Juan, J. C.; Johan, M. R. Advanced Photocatalytic Degradation of Acetaminophen Using Cu2O/WO3/TiO2 Ternary Composite under Solar Irradiation. *Catal. Commun.* **2022**, *163*, No. 106396.

(63) Ranjith Kumar, D.; Ranjith, K. S.; Haldorai, Y.; Kandasami, A.; Rajendra Kumar, R. T. Nitrogen-Implanted ZnO Nanorod Arrays for Visible Light Photocatalytic Degradation of a Pharmaceutical Drug Acetaminophen. *ACS Omega* **2019**, *4* (7), 11973−11979.

(64) Hassan, F.; Backer, S. N.; Almanassra, I. W.; Ali Atieh, M.; Elbahri, M.; Shanableh, A. Solar-Matched S-Scheme ZnO/g-C3N4 for Visible Light-Driven Paracetamol Degradation. *Sci. Rep.* **2024**, *14* (1), 12220.

(65) Blangetti, N.; Freyria, F. S.; Calviello, M. C.; Ditaranto, N.; Guastella, S.; Bonelli, B. Photocatalytic Degradation of Paracetamol under Simulated Sunlight by Four TiO2 Commercial Powders: An Insight into the Performance of Two Sub-Micrometric Anatase and Rutile Powders and a Nanometric Brookite Powder. *Catalysts* **2023**, *13* (2), 434.